Modelling the stress/strain behavior of sand using a multi-surface kinematic model

D. V. Griffiths and J. H. Prevost
Department of Civil Engineering
Princeton University
Princeton, N.J. 08544

Abstract

The paper discusses the performance of a multi-surface kinematic model for sand [1] when compared against actual laboratory data for various stress paths. Methods of parameter identification are described, and the data presented for calibration of the model assessed. Suggestions are also made for possible improvements to the model.

1. INTRODUCTION

A recent workshop [2] on granular materials presented the opportunity for soil modellers to assess the performance of their models against actual test data. The idea of the workshop was that modellers would first be presented with data on two different sands. These data had been obtained from conventional laboratory tests (ie. compression, extension, hydrostatic) and these were to be used to identify the parameters and calibrate the models. Following parameter identification, the modellers were asked to use their models to make predictions of the response of the same sands to rather more complex stress paths. After submission of the 'blind' predictions, the actual test results for these same stress paths were made available so that modellers could tell how well (or badly!) their model had performed.

This paper assesses the data made available for parameter identification, and reviews the subsequent predictions made in the light of the laboratory 'results'.

2. THE SANDS UNDER ANALYSIS

The two sands were given the names 'Hostun' and 'Reid', and were both poorly graded (SP) materials with similar grain size distributions [2]. A summary of the densities of the two sands is given in Table 1. It is apparent that the Hostun and Reid sands were tested at 97% and 43% relative densities respectively.

Table 1. Summary of soil densities.

	HOSTUN	REID
% Sand	99.6	99.4
Specific Gravity	2.67	2.65
Max. Density (g/cm^3)	1.66	1.74
Min. Density (g/cm^3)	1.35	1.46
Set-up Density (g/cm^3)	1.65	1.58
% Relative Density	97	43

3. TESTING DEVICES

Each of the sands was made to follow 'identical' stress paths using both a hollow cylinder and a cubical device. A more detailed description of these devices is to be found in reference 2, but their main features will now be summarized.

3.1 Hollow Cylinder

The samples were prepared dry and then fully saturated to allow for volume change measurements to be made. All tests started from an initial hydrostatic state of stress ($\sigma_r = \sigma_z = \sigma_\theta$) and were fully drained. In all the tests, the same stress was applied to the inner and outer surfaces of the hollow cylinder, and this stress $\sigma_r\,(=\sigma_\theta)$ was always the intermediate principal stress. A 'compression' test was performed by increasing the axial stress σ_z to

failure and an 'extension' test was performed by reducing σ_z to failure.

The stress paths to be followed in the predictions involved increasing or decreasing the axial stress σ_z while applying a torsional stress $\tau_{z\theta}$, such that the ratio of these two quantities remains constant. This can be expressed in terms of an angle β where

$$\tan^2\beta = \frac{2\tau_{z\theta}}{\Delta\sigma_z - \Delta\sigma_\theta} \qquad (1)$$

This angle represents the inclination of the major and minor principal stresses to the vertical and horizontal directions. In tests where the cell pressure is not changed, this expression simplifies to

$$\tan^2\beta = \frac{2\tau_{z\theta}}{\Delta\sigma_z} \qquad (2)$$

where $\Delta\sigma_z$ represents the change in axial stress from its initial hydrostatic value.

A stress path in which β is constant can be expressed in two other ways; firstly, assuming σ_1, σ_2 and σ_3 are the largest, intermediate and smallest compressive principal stresses respectively, we define the parameter b where

$$b = (\sigma_2 - \sigma_3)/(\sigma_1 - \sigma_3) \qquad (3)$$

hence

$$b = \sin^2\beta , \qquad (4)$$

and secondly defining the Lode Angle θ where

$$\theta = \tan^{-1}((1 - 2b)/\sqrt{3}) \qquad (5)$$

we get

$$\theta = \tan^{-1}((1 - 2\sin^2\beta)/\sqrt{3}) \qquad (6)$$

For a compression - negative sign convention, the following limiting values are implied -

	Extension	Compression
β	90°	0
b	1	0
θ	−30°	30°

When viewed in a deviatoric plane, a constant β stress path appears as a straight line moving away radially from the space diagonal.

For each sand, six hollow cylinder tests were performed as summarized in Table 2. For each sand, two compression and two extension tests were

Table 2. Summary of Hollow Cylinder data.

Sand Name	Data Name	p_o kPa	Type of Test
HOSTUN	HH1	203	Compression
	HH2	500	Compression
	HH3	203	Extension
	HH4	500	Extension
	HH5	350	Compression (unload/reload)
	HH6	69	Hydrostatic (unload/reload)
REID	HR1	345	Compression
	HR2	483	Compression
	HR3	345	Extension
	HR4	483	Extension
	HR5	207	Compression (unload/reload)
	HR6	103	Hydrostatic (unload/reload)

performed at different initial confining stresses. In addition, a compression test and a hydrostatic test were performed, both with loading followed by unloading.

3.2 Cubical Device

The cubical tests were performed on dry samples of sand. The specimen was deformed between six rigid platens with no gap between them. The nominal size of the cube was 10 cm x 10 cm x 10 cm. The normal (principal) stresses applied in each direction were measured by pressure cells embedded in the platens. Deformations were measured using LVDT's. All the data summarized in Table 3 was obtained in a stress controlled environment, although strain control could have been used.

Compression tests were performed by increasing the vertical stress σ_z and extension tests were performed by reducing the axial stress, in both cases keeping the other stresses constant. The cubical device allows virtually any stable stress path to be followed. A constant b or (β) can be achieved by altering σ_x and σ_z while keeping σ_y constant. If a 'compression' test with constant b is performed, $\sigma_z = \sigma_1$ and $\sigma_x = \sigma_3$, otherwise in 'extension' $\sigma_x = \sigma_1$ and $\sigma_z = \sigma_3$ (assuming that $\sigma_1 \geq \sigma_2 \geq \sigma_3$). If the initial hydrostatic stress is given by p_o we get

$$b = \frac{p_o - \sigma_3}{\sigma_1 - \sigma_3} \qquad (7)$$

hence

$$\sigma_3 = \frac{1}{(1-b)}(p_o - b\sigma_1) \qquad (8)$$

A 'circular' stress path can be followed using the cubical device by altering the three principal stresses in such a way that the mean stress p and the radial distance from the space diagonal t remain constant where

$$p = \frac{1}{3}(\sigma_1 + \sigma_2 + \sigma_3) \qquad (9)$$

$$t = (2J_2)^{\frac{1}{2}} \qquad (10)$$

$$= \frac{[(\sigma_1-\sigma_2)^2+(\sigma_2-\sigma_3)^2+(\sigma_3-\sigma_1)^2]^{\frac{1}{2}}}{\sqrt{3}}$$

From Tables 2 and 3 it can be seen that the same sequence of tests was performed using both testing devices. The exception was the case of hydrostatic loading/unloading for the Hostun Sand where the hollow cylinder test (HH6) started at a smaller initial stress value than the cubical test (CH6).

Table 3. Summary of Cubical Device data.

Sand Name	Data Name	p_o kPa	Type of Test
HOSTUN	CH1	200	Compression
	CH2	500	Compression
	CH3	200	Extension
	CH4	500	Extension
	CH5	350	Compression (unload/reload)
	CH6	100	Hydrostatic (unload/reload)
REID	CR1	345	Compression
	CR2	483	Compression
	CR3	345	Extension
	CR4	483	Extension
	CR5	207	Compression (unload/reload)
	CR6	100	Hydrostatic (unload/reload)

4. GENERAL OBSERVATIONS ON THE DATA

An initial survey of the data summarized in Tables 2 and 3 was performed to check that it was behaving in a consistent and reproducible manner.

4.1 Peak Friction Angle

By observing the peak shear stress in the tests, a value of the Mohr-Coulomb friction angle could be back-figured. These values are summarized in Table 4 where both the peak friction angle ϕ and the mean stress at 'failure' are given. A rather con-

Table 4. Peak and critical friction angles ϕ' and ϕ_μ.

Sand Name	Test	ϕ'	p kPa	ϕ_μ
HOSTUN	HH1	40	443	31
	HH2	38	1036	31
	CH1	40	445	33
	CH2	38	1043	28
	HH3	45	147	29
	HH4	41	368	29
	CH3	53	141	
	CH4	45	362	
REID	HR1	34	639	29
	HR2	34	882	30
	CR1	34	640	27
	CR2	32	855	28
	HR3	38	257	31
	HR4	37	362	29
	CR3	39	256	26
	CR4	43	352	35

sistent picture emerges in which the Hostun and Reid Sands have peak friction angles in compression of around 40° and 34° respectively. Even if both sands were identical, the Hostun Sand would be expected to have a higher friction angle due to its very high relative density (Table 1). The friction angles from the extension tests are generally a few degrees higher and more sporadic as would be expected. Extension tests are inherently less stable than compression tests due to 'necking' at failure.

4.2 Critical Friction Angle

The 'critical' friction angle ϕ_μ is defined here as the mobilised friction angle corresponding to zero volume change during shear. This situation occurs when volumetric compaction ceases and ditation begins. Zero volume change conditions also occur at 'large' strains when the sand reaches its 'residual' strength, but data on this condition was not available. By observing the onset of dilation in the data, the Hostun sand gave $28° < \phi_\mu < 30°$ and the Reid sand gave $26° < \phi_\mu < 35°$, also shown in Table 4. The exception occurred in tests CH3 and CH4 where dilation appeared to start immediately upon shearing.

These values are quite acceptable as it is well known [3] that ϕ_μ for most soils corresponds to a mobilised stress ratio $\dfrac{\sigma_1}{\sigma_3} \approx 3$ or $\phi_\mu \approx 30°$.

4.3 Initial Stiffness

For each compression test, the initial stiffness over the first 10 steps was obtained as a secant modulus. The stiffness was calculated using

$$\frac{\sigma_z - \sigma_{x(r)}}{\varepsilon_z - \varepsilon_{x(r)}} = 2G \qquad (11)$$

and summarized in Table 5 together with the average mean stress over the first 10 steps.

This data set did not always give the positive correlation between mean stress and stiffness that would be expected for granular soils. For example HR1 was less stiff than HR5 in spite of HR5 being performed at a lower mean stress as shown in Figure 1. This negative correlation was also observed in the cubical results between tests CR2 and CR1.

It was also observed from Table 5 that stiffnesses measured in the hollow cylinder device were invariably greater than in the cubical device. For example consider tests HR5 and CR5. Both tests were performed at the same initial stress of 207 kPa and the secant stiffness was measured over a similar range of mean stress. The stiffness measured in the hollow cylinder however is 2.7 times greater than that measured in the cubical device over the first 10 steps. Part of the problem is explained in Figure 2 where the first 10 steps of both tests have been plotted. The cubical results show considerably more experimental 'noise' than the hollow cylinder results suggesting that the secant modulus value obtained from this data would be rather unreliable.
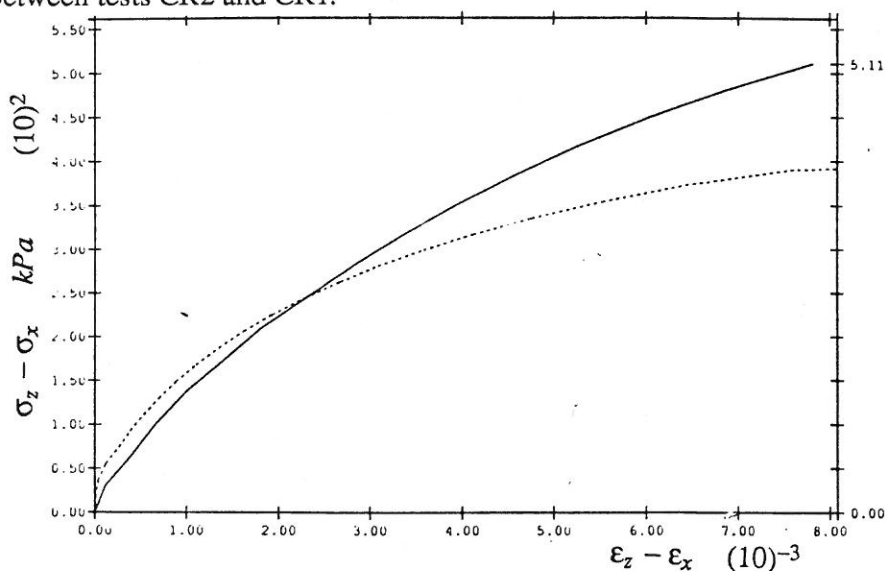

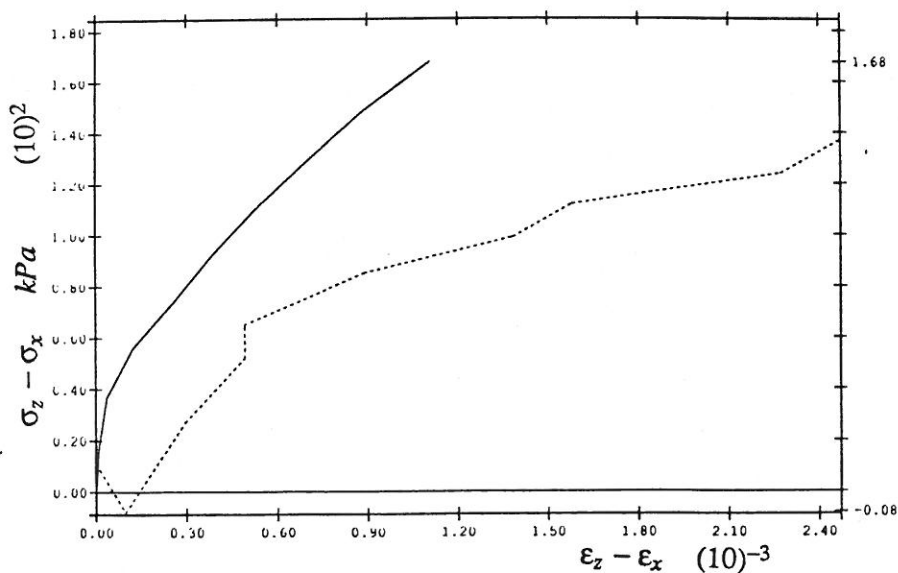Figure 1.   Comparison of HR1 (solid), $p_o = 345$ kPa and HR5 (dashed), $p_o = 207$ kPa.

Figure 2.   Comparison of HR5 (solid) and CR5 (dashed), both $p_o = 207$ kPa.

Table 5. Initial stiffness data.

Test	p_{av}	$2G$	p_o
HH1	247	1.26E5	203
CH1	273	0.50E5	200
HH5	399	1.41E5	350
CH5	398	0.75E5	350
HH2	598	1.43E5	500
CH2	568	1.13E5	500
HR5	235	1.51E5	206
CR5	229	0.55E5	207
HR1	398	0.94E5	345
CR1	427	0.62E5	345
HR2	555	1.83E5	483
CR2	634	0.47E5	483

4.4 Overall Comparison of Hollow Cylinder and Cubical Data

Figures 3-6 show comparisons of the hollow cylinder (solid) and cubical data (dashed) for the compression tests. The plots are of axial stress (σ_z) vs. axial strain (ε_z) and volumetric strain ($\varepsilon_v = \varepsilon_{x(r)} + \varepsilon_{y(z)} + \varepsilon_{z(\theta)}$) vs. axial strain. Although the results are generally similar, the differences are occasionally significantly large, and raise fundamental questions about the testing procedures used. Although the cubical results are always more 'noisy' than their hollow cylinder counterparts, the 'noise' is not sufficient to explain the differences observed. From a statistical viewpoint, the σ_z vs. ε_z results in compression for the Hostun sand (Figures 3 and 4) differ so much that it is highly unlikely that the two curves come from the same 'population'. On the other hand, the volumetric behavior, which is usually considered to be a rather hard quantity to measure accurately, shows much better agreement between the two devices. Even so, the comparison between HR2 and CR2 shows poor agreement (Figure 6) with respect to volumetric changes, but rather good agreement for σ_z vs. ε_z.

5. MODEL CALIBRATION AND PARAMETER IDENTIFICATION

It was observed that the predictions for the Hostun and Reid sands were all to be conducted with initial stress states of 500 kPa and 345 kPa respectively. The data used to generate the parameters for these tests were therefore chosen to be HH2

and HH4 for the Hostun and HR1 and HR3 for the Reid as these were at the corresponding initial stress levels.

In both cases, the model took the form of a set of nested conical yield surfaces with their apexes at the origin. It is up to the modeller as to how many surfaces are to be incorporated, but in the present case a rather detailed descretisation of the stress/strain curves resulted in 27 and 23 surfaces for the Hostun and Reid models respectively.

The parameter identification procedure has the important property of being <u>user independent</u>. A program called MUD [4] generates all the necessary parameters on being fed the raw data in the form of triaxial extension and compression curves.

The projection of the cones on any deviatoric plane in principal stress space gives a circle whose centre does not necessarily coincide with the space diagonal. This implies that the surfaces are not right circular cones but actually have an elliptical crossection when viewed down their 'axes'.

The innermost cone represents the limit of purely elastic behavior and the outermost cone the failure surface, outside which no stresses can exist legally. Each cone carries with it four basic parameters α, k, H_C' and H_E' where -

α = tensor defining the centre of the circle on the deviatoric plane corresponding to the reference pressure p_0.

k = radius of the circle in that place

H_C', H_E' = plastic moduli in compression and extension.

The outermost cone has the largest radius with $H_C' = H_E' = 0$. As yielding takes place, all cones except the outermost cone can be translated by the stress point in principal stress space. The model is 'non-associated' with the sign of the volumetric changes governed by the value of the stress ratio given by -

$$\eta = \frac{q}{p} \qquad (12)$$

where

$$q = |\sigma_1 - \sigma_3|$$
$$p = (\sigma_1 + \sigma_2 + \sigma_3)/3$$

This critical stress ratio ($\overline{\eta}$) is typically set to 1.2 in compression and 0.857 in extension (equivalent to
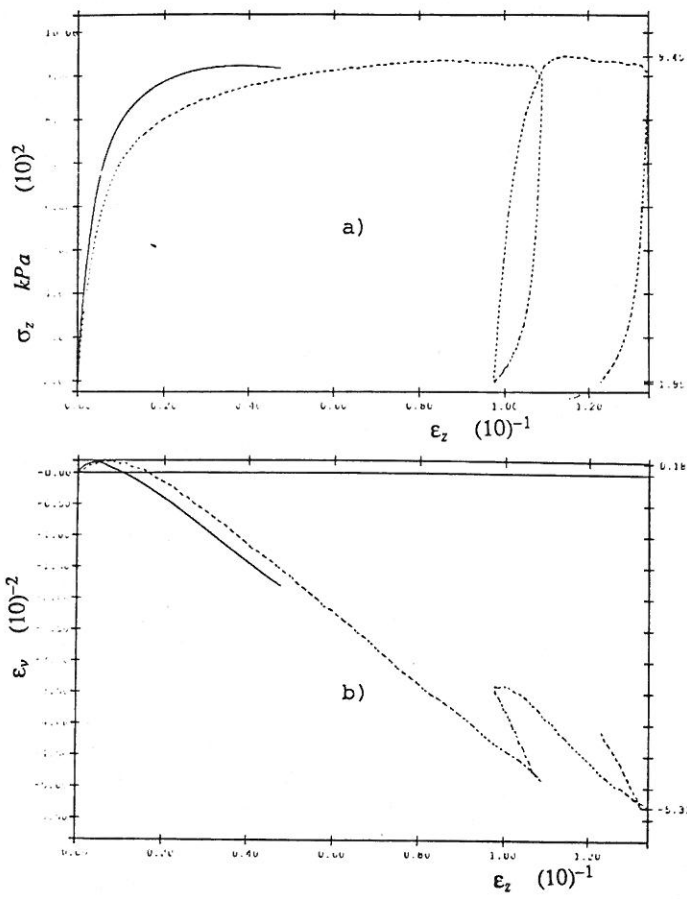
Figure 3. Comparison of HH1 (solid) and CH1 (dashed) data, a) axial stress, b) volumetric strain.
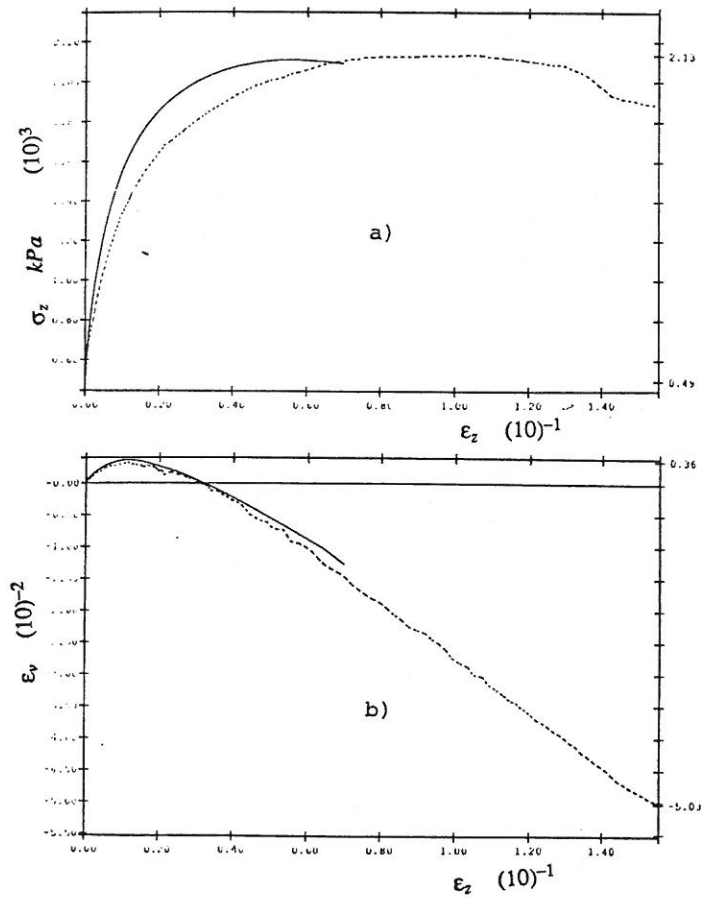

Figure 4. Comparison of HH2 (solid) and CH2 (dashed) data, a) axial stress, b) volumetric strain.
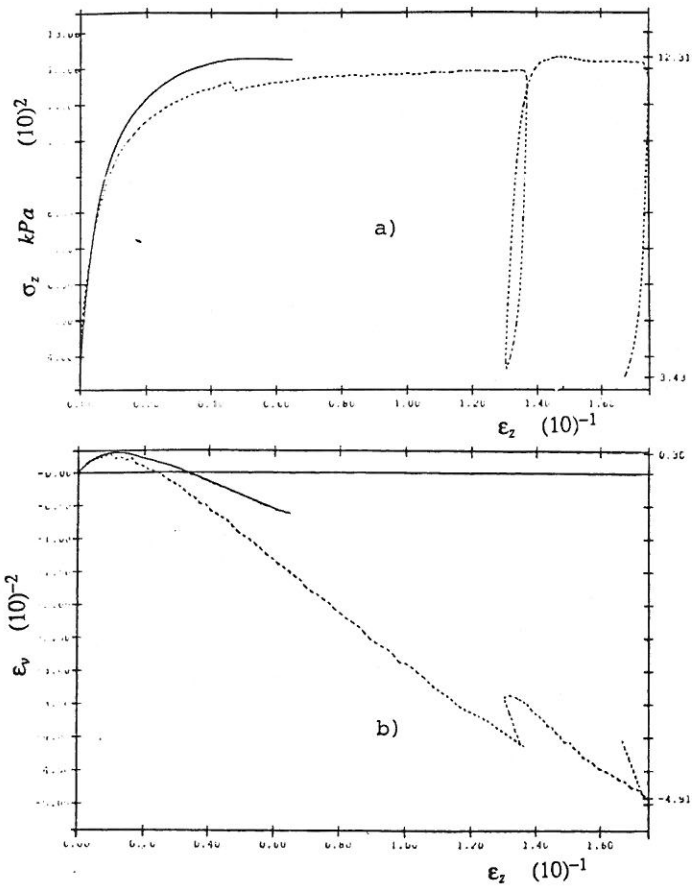
Figure 5. Comparison of HR1 (solid) and CR1 (dashed) data, a) axial stress, b) volumetric strain.
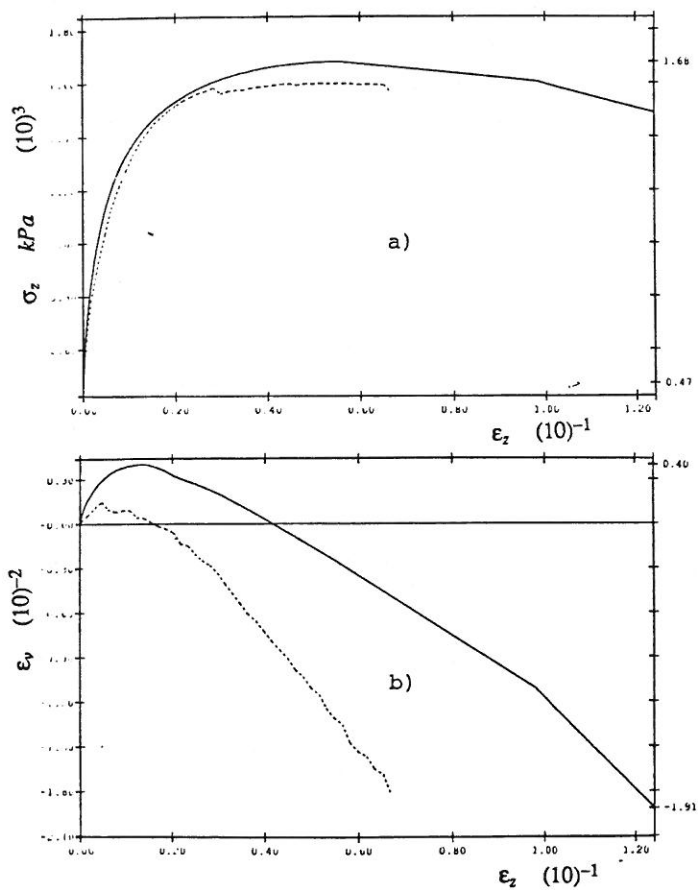

Figure 6. Comparison of HR2 (solid) and CR2 (dashed) data, a) axial stress, b) volumetric strain.

$\sigma_1/\sigma_3 = 3$ in terms of principal stresses). Shearing that occurs at stress ratios lower than the critical value result in volume decrese or compaction and shearing that occurs at stress ratios higher than the critical value results in volume increase or dilation. For more details of the model, the reader is referred to reference 1.

6. STRESS DRIVEN ALGORITHM

The frictional model is implemented by a second program called TESTA [5] which drives the 'Stress point Algorithm' [6], maintaining user independence. Details of the Stress Point Algorithm used to obtain the predictions are beyond the scope of this paper. It may be noted however, that the basic algorithm is strain-driven and uses an explicit (Euler) one-step approach which numerically integrates the elasto-plastic rate equations and given increments of strain returns the corresponding increments of stress through a relationship of the form-

$$\Delta\sigma = \int_0^{\Delta\varepsilon} \mathbf{D}^{ep} \, d\varepsilon \qquad (13)$$

All the predictions required in the present work were stress-driven, hence equation (13) could not be used directly. In the present work an iterative approach [5] is used as outlined in Table 6. Hence stress increments $\Delta\sigma$ are provided, and after some iterations, the corresponding strain increments $\Delta\varepsilon$ are obtained. Typically, an upper limit on the number of iterations would be imposed, and a dimensionless convergence criterion applied to stop iterations once a certain tolerance was reached.

7. PREDICTIONS AND COMPARISONS WITH MEASURED VALUES

A total of twelve predictions were requested with six corresponding to each testing device. Of the six predictions from each device, three were for Hostun and three for Reid. Nine predictions were attempted by the authors, and these are now described. All the predictions are compared with test results at the back of this report.

7.1 Hostun Sand

7.1.1 Prediction PHH1 (compression, b = 0.286)

From an initial spherical stress state of 500 kPa, the shear stress $\tau_{z\theta}$ was increased to 450 kPa while the axial stress (σ_z) was increased proportionately by 426.2 kPa to 926.2 kPa. The three plots labelled HH1 give the shear stress $(\tau_{z\theta})$, the

Table 6. Stress driven algorithm.

PROBLEM STATEMENT:

- *GIVEN:* the converged state $(\sigma_n, \varepsilon_n^p)$ and the stress increment $\Delta\sigma$,

- *FIND:* the corresponding strain increment $\Delta\varepsilon$, such that:

$$\sigma_{n+1} = \sigma_n + \int_0^{\Delta\varepsilon} \mathbf{D}^{ep} \, (\sigma, \varepsilon^p) : d\varepsilon = \sigma_n + \Delta\sigma$$

where:

$$\mathbf{D}^{ep} : d\varepsilon = \mathbf{E} : d\varepsilon - \mathbf{E} : \mathbf{P} < \frac{\mathbf{Q} : \mathbf{E} : d\varepsilon}{H' + H_0} >$$

ALGORITHM:

(1) Initialize:

$i = 0$

$\Delta\varepsilon^{(0)} = \mathbf{E}^{-1} : \Delta\sigma$

(2) Iterative Phase:

1. $\sigma_{n+1}^{(i)} = \sigma_n + \int_0^{\Delta\varepsilon^{(i)}} \mathbf{D}^{ep} : d\varepsilon \leftarrow$ Stress Point Algo.

2. $\Delta\sigma^{(i)} = \sigma_{n+1} - \sigma_{n+1}^{(i)}$

3. *IF* $(\, | \, \Delta\sigma^{(i)} / \Delta\sigma \, | \leq TOL \,) \quad \Delta\varepsilon = \Delta\varepsilon^{(i)} \rightarrow END$

   ELSE:

4. $\Delta\varepsilon^{(i+1)} = \Delta\varepsilon^{(i)} + \mathbf{E}^{-1} : \Delta\sigma^{(i)}$

   $i = i + 1; \quad GOTO \ 1.$

Typically: $TOL = 10^{-6}$.

volumetric strain (ε_v) and the axial strain (ε_z) plotted against the shear strain $(\gamma_{z\theta})$.

The HH1 predictions are in excellent agreement, but the model predicts less dilation than was observed in the experimental results.

7.1.2 Prediction PHH2 (extension, b = 0.667)

From an initial spherical stress state of 500 kPa, the shear stress $(\tau_{z\theta})$ was increased to 270 kPa while the axial stress (σ_z) was reduced proportionately by 198.4 kPa to 301.6 kPa. Three plots labelled HH2 give the shear stress $(\tau_{z\theta})$ the volumetric strain (ε_v) and the axial strain (ε_z) plotted against the shear strain $(\gamma_{z\theta})$.

The HH2 predictions overestimate the shear stiffness and strength. The model also appears to show considerable dilation, whereas the experimental data seems reluctant to dilate at all ! The volumetric behavior of HH1 and HH2 are worthy of further comment in view of the extremely high relative density of the Hostun sample being tested (97%). Such a dense material would be expected to show very little volumetric compaction prior to

dilation. This is especially true in the extension test, where the mean stress is falling. In the compression test, where the mean stress is rising, a little additional volumetric compaction can be expected due to grain crushing. It is therefore apparent that qualitatively, the predicted volumetric behavior shows a more consistent pattern than the experimental.

7.1.3 Prediction PHH3 (cyclic, b variable)

From an initial spherical stress state of 500 kPa, the stress path is split into three stages -
a)   Increase σ_z by 520 kPa to 1020 kPa keeping all other stresses constant
b)   Apply five full cycles of $\tau_{z\theta}$ with amplitude 136 kPa keeping all other stresses constant
c)   Increase $\tau_{z\theta}$ to 450 kPa keeping all other stresses constant.

The three plots labelled HH3B correspond to phase b) above, and the two plots labelled HH3C to phase c). In HH3C, the volumetric strain and shear strain have been shifted so that they start at the origin.

In the cyclic loading predictions of HH3B, the shear stress/strain plots were in reasonable agreement although the predicted behavior showed hardly any change from one cycle to the next. The stiffening effects of cycling on the experimental results was quite apparent, especially between the first and second cycles.

A shortcoming of the model is apparent in the volumetric and axial strain plots of HH3B. Whereas the experimental results 'shake down' to a converged value of strain after a few cycles, the model predicts ever-increasing volumetric changes with each cycle. This problem will be addressed in the next section.

After cycling, the strains were brought back to the origin, and the sample sheared monotonically to failure. The shear stresses predicted by HH3C agree rather well with experimental values, but the model predicts less dilation than was observed.

7.1.4 Prediction PCH1 (compression, b=0.286)

From an initial spherical stress state of 500 kPa, the axial stress (σ_z) was increased by 600kPa to 1100kPa while the lateral stress (σ_x) was decreased proportionately by 240.3kPa to 259.7 kPa (see equation 8). The other lateral stress (σ_y) was kept constant. The plots labelled CH1 show the three strains $\varepsilon_x, \varepsilon_y$ and ε_z plotted against the dimensionless shear stress level $\frac{t}{p}$ (SD2/S1). In the lower figure the volumetric strain (ε_v) is plotted against $\frac{t}{p}$.

The strains in CH1 agree well with the experimental values up to about 65% of the ultimate load. Thereafter, the predicted values overestimate the observed strength of the soil and continue to harden. The volumetric behavior was not in particularly good agreement with experiment.

7.1.5 Prediction PCH2 (extension, b=0.666)

From an initial spherical stress state of 500 kPa, the axial stress (σ_z) was reduced by 330 kPa to 270 kPa while the lateral stress (σ_x) was increased proportionately by 165.5 kPa to 665.5 kPa (see equation 8). The other lateral stress (σ_y) was kept constant. The plots labelled CH2 show the three strains $\varepsilon_x, \varepsilon_y$ and ε_z plotted against the dimensionless shear stress level $\frac{t}{p}$ (SD2/S1). In the lower figure the volumetric strain (ε_v) is plotted against $\frac{t}{p}$.

The initial stiffness of the soil was modelled well in CH2, but the predictions were terminated before a failure load could be defined. The model predicted immediate dilation on shearing in extension, which is to be expected in such a dense sample. The experimental data however, showed a certain amount of compaction prior to dilation.

7.1.6 Prediction PCHC (circular path)

From an initial spherical stress state of 500 kPa, the stress path is split into two stages -
a)   The axial stress (σ_z) is increased by 343 kPa to 843 kPa while σ_x and σ_y are both reduced proportionately by 171 kPa to 329 kPa, maintaining the mean stress p at 500 kPa. The deviatoric stress invariant t finally becomes equal to 420 kPa.
b)   The three stresses σ_x, σ_y and σ_z are varied sinusoidally but out of phase in such away that a circular stress path is followed in a deviatoric plane where p and t remain constant. The plots labelled CHC show the variation of the three strains and the volumetric strain against the strain invariant Φ_σ (analogous to t for stresses). Finally, a plot is given in principal strain space of the path followed in a deviatoric plane.

The circular path predictions of CHC showed

poor agreement with the experimental results. The experimental results indicated that the material followed strain paths that were broadly similar to the stress paths applied to the sample. Yielding was observed during the circular path, whereas the model gave virtually no accumulation of strain.

7.2 Reid Sand

7.2.1 Prediction PHR1 (compression, b = 0.277)

From an initial spherical stress state of 345 kPa, the shear stress $(\tau_{z\theta})$ was increased to 280 kPa while the axial stress (σ_z) was increased proportionately by 279.1 kPa to 624.1 kPa. The three plots labelled HR1 give the shear stress $(\tau_{z\theta})$ the volumetric strain (ε_v) and the axial strain (ε_z) plotted against the shear strain $(\gamma_{z\theta})$.

The comments applicable to this section are very similar to those made previously for the Hostun sand. The compression predictions in HR1 were rather good although the model underestimated the dilation.

7.2.2 Prediction PHR2 (extension, b = 0.723)

From an initial spherical stress state of 345 kPa, the shear stress $(\tau_{z\theta})$ was increased to 140 kPa while the axial stress (σ_z) was reduced proportionately by 139.5 kPa to 205.5 kPa. Three plots labelled HR2 give the shear stress $(\tau_{z\theta})$ the volumetric strain (ε_v) and the axial strain (ε_z) plotted against the shear strain $(\gamma_{z\theta})$.

The extension predictions in HR2 tended to be over-stiff and the model overestimated the dilation. The Reid sand was set-up as a 'loose' material with a relative density of 43% and would therefore be expected to show volumetric compaction prior to dilation. It is not clear, however, why the experimentally obtained volumetric compaction for this sand was greater in extension than compression.

7.2.3 Prediction PHR3 (cyclic, b variable)

From an initial spherical stress state of 345 kPa, the stress path is split into three stages -

a) Increase σ_z by 283.0 kPa to 628.0 kPa keeping all other stresses constant.

b) Apply five full cycles of $\tau_{z\theta}$ with amplitude 93 kPa keeping all other stresses constant.

c) Increase $\tau_{z\theta}$ to 280 kPa keeping all other stresses constant.

The three plots labelled HR3B correspond to phase b) above and the two plots labelled HR3C to phase c). In HR3C, the volumetric strain and shear strain have been shifted so that they start at the origin.

The cyclic results in HR3B show a similar behavior to that obtained previously. The predicted shear stress/strain plot is less stiff than the experimentally obtained results and shows less variation from one cycle to the next. The experimentally obtained shear strain does not appear to 'shaking-down' as much as would be expected for a loose material. Furthermore, a form of instability is apparent in the experimental data where the fifth cycle indicates an increased amount of shear strain over the fourth cycle.

After cycling, the strains were brought back to the origin, and the sample sheared monotonically to failure. The shear stresses predicted by HR3C agree rather well with experimental values, but the model predicts less dilation than was observed.

8. SUGGESTED IMPROVEMENTS TO THE MODEL

8.1 Shake-down

The most important deficiency of the model highlighted by the predictions was its inability to 'shake-down' during cyclic loading. Theoretically, a loose sand sample will compact if subject to cycles of shear stress at a stress ratio below the critical value. As the sample densifies however, the tendency for compaction will reduce even though the amplitude of shear stress cycling is held constant. Eventually, the sample reaches a maximum density where further compaction is impossible. If such a dense sample is sheared monotonically, essentially no volume change would take place until a stress ratio $\dfrac{\sigma_1}{\sigma_3} \approx 3$ was reached, when the sample would dilate.

In order to reproduce this behavior, the model needs to keep track of the relative density of the sample as cycling proceeds. Incorporation of the maximum and minimum porosities of the sand (n_{max}, n_{min}) and the initial porosity at which the sample is prepared (n_o), leads to the initial relative density given by-

$$D_r = \frac{n_{max} - n_o}{n_{max} - n_{min}} \qquad (14)$$

During cycling, volume changes can be converted into changes in porosity through the rate equation-

$$\frac{\dot{n}}{1 - n} = \dot{\varepsilon}_v \qquad (15)$$

Hence, if n_o is the initial porosity and the change in volumetric strain is given by $\Delta\varepsilon_v$ (compression positive), then the new porosity n_1 is given by-

$$n_1 = 1 - (1 - n_o)\, e^{-\Delta\varepsilon_v} \qquad (16)$$

from which the relative density can be updated.

The volume change in the model should be made a function of both the stress ratio (η) and the relative density (D_r). The present [1] volumetric relationship is of the form-

$$\Delta\varepsilon_v = f(\eta/\bar{\eta})$$
$$= ((\eta/\bar{\eta})^2 - 1)/((\eta/\bar{\eta})^2 + 1) \quad (17)$$

where $\eta < \bar{\eta}$ corresponds to compaction and $\eta \geq \bar{\eta}$ corresponds to dilation. The proposed volumetric relationships will be of the form-

$$\eta < \bar{\eta} \quad \Delta\varepsilon_v = g(1 - D_r)\, f(\eta/\bar{\eta}) \quad (18)$$
$$\eta \geq \bar{\eta} \quad \Delta\varepsilon_v = h(D_r)\, f(\eta/\bar{\eta}) \quad (19)$$

The most effective form of the functions g and h has yet to be determined.

8.2 Prediction of Failure Loads

During some of the predictions, the model overshot the observed strength of the samples. The reasons for this have yet to investigated, but it is possibly related to the deficiencies of a circular conical failure surface [7]. The model is anchored in triaxial compression and extension, so the failure stress ratio at intermediate locations is not fully controlled. The model has the facility to alter the shape of the failure surface to approximate more closely the Mohr-Coulomb surface through a simple data change, and this could be investigated.

8.3 Circular Path

In common with many predictors, the model failed to reproduce the circular path behavior observed experimentally. The reasons for this are not clear at present, but it is likely to be related to problems associated to the stress driven algorithm (Table 6) rather than the model itself. It is felt that the circular stress path is a severe test of the stress driven algorithm, especially when the yield surfaces are also circular. This neutral loading condition could be avoided by a change in shape of the yield surfaces, which would also have the effect of generating more plastic strain.

9. CONCLUSIONS

Data has been provided on the stress/strain properties of two sands which have been used to calibrate a multi-surface kinematic model. The predictions made using the model are presented at the end of this report. Implementation of the model is user-independent, which is an important consideration for any model if it is to be used with confidence. The predictions for both monotonic and cyclic loading paths were generally good, although some deficiencies of the model were highlighted.

The data provided for model calibration has also been assessed. It was found that anomalies existed both within and between the two testing devices. This raises once more the problem of accuracy and reproducibility of soil test data. It is suggested that one of the most useful objectives of the soil testing data bank would be to enable levels of confidence to be established for data obtained from different testing devices.

10. ACKNOWLEDGMENTS

11. REFERENCES

1. **Prevost,J.H.** "A simple plasticity theory for frictional cohesionless soils." *Soil Dynamics and Earthquake Engineering*, vol.4, No.1, 1985, pp.9-17.

2. **Saada,A.S. (Editor)** "International workshop on constitutive equations for granular non-cohesive soils." Information Package, Case Western reserve University, July 1987.

3. **Rowe,P.W.** "Theoretical meaning of and observed values of deformation parameters for soil." Proceedings of the Roscoe Memorial Symposium, Cambridge, U.K., 1971, pp.548-563.

4. **Prevost,J.H.** "TESTA: A computer program to test constitutive behavior of nonlinear,anisotropic,hysteretic materials." Dept. of Civil Engineering, Princeton University, June 1980 (last update Sep 1986).

5. **Prevost,J.H.** "MUD: A computer program to compute the model parameters for elasto-plastic material models." nonlinear,anisotropic,hysteretic materials." Dept. of Civil Engineering, Princeton University, Mar 1981 (last update Sep 1986).

6. **Prevost,J.H.** "Mechanics of dissipative media-Lecture notes." Dept. of Civil Engineering, Princeton University, Jun 1987.

7. **Griffiths,D.V.** "Some theoretical observations on conical failure criteria in principal stress space." *Int. J. Solids Structures* ,vol.22,no.5,pp.553-565,(1986).